Flight Demonstration of High Altitude Aircraft Navigation With Cellular Signals

IMAGE LICENSED BY INGRAM PUBLISHING

Zaher (Zak) M. Kassas*
Is with the Department of Electrical and Computer Engineering, The Ohio State University, Columbus, OH 43210 USA.
E-mail: zkassas@ieee.org

Joe Khalife and Ali A. Abdallah
Were with the Autonomous Systems Perception, Intelligence, and Navigation Laboratory, University of California, Irvine CA 92697 USA.
E-mail: khalifej@uci.edu; abdalla2@uci.edu

Digital Object Identifier 10.1109/MITS.2023.3236890
Date of current version: 9 May 2023

*Corresponding author

1939-1390/23©2023IEEE

Chiawei Lee, Juan Jurado, Steven Wachtel, Jacob Duede, Zachary Hoeffner, Thomas Hulsey, and Rachel Quirarte

Are with the Test Pilot School, U.S. Air Force, Edwards Air Force Base, Edwards, CA 93524 USA. E-mail: chiawei.lee@us.af.m; jdjurado@icloud.com; steven.wachtel.1@us.af.mil; jacob.duede@us.af.mil; zachary.hoeffner.1@us.af.mil; thomas.hulsey.2@us.af.mil; rachel.quirarte@us.af.mil

RunXuan Tay

Is with the Air Warfare Center, Republic of Singapore Air Force, Singapore. E-mail: rxtay@outlook.com

Abstract—This article presents the first demonstration of navigation with cellular signals of opportunity (SOPs) on a high-altitude aircraft. An extensive flight campaign was conducted by the Autonomous Systems Perception, Intelligence, and Navigation Laboratory in collaboration with the U.S. Air Force to sample ambient downlink cellular SOPs in different regions in Southern California, USA. Carrier phase measurements were produced from these signals, which were subsequently fused in an extended Kalman filter along with altimeter measurements to estimate the aircraft's state (position, velocity, and time). Three flights are performed in three different regions: 1) rural, 2) semiurban, and 3) urban. A multitude of flight trajectories and altitudes above ground level (AGL) was exercised in the three flights: 1) a 51-km trajectory of grid maneuvers with banking and straight segments at about 5,000 ft AGL, 2) a 57-km trajectory of a teardrop descent from 7,000 ft AGL down to touchdown at the runway, and 3) a 55-km trajectory of a holding pattern at about 15,000 ft AGL. The estimated aircraft trajectory is computed for each flight and compared with the trajectory from the aircraft's onboard navigation system, which utilized a GPS receiver coupled with an inertial navigation system and an altimeter. The cellular SOPs produced remarkable sustained navigation accuracy over the entire flight trajectories in all three flights, achieving a 3D position root mean-squared error of 10.53 m, 4.96 m, and 15.44 m, respectively.

Introduction

A quick search of the phrase "Global Positioning System (GPS)" on the Aviation Safety Reporting System (ASRS) returns 579 navigation-related incidents since January 2000. The ASRS is a publicly available reporting system established by NASA to identify and address issues reported by frontline personnel in the aviation system [1]. A deeper look at the data reveals that, out of these 579 incidents, a malfunction or failure was detected in navigation sensors with the following occurrences: 508 in "GPS & Other Satellite Navigation," 34 in "Navigational Equipment and Processing," 14 in "Flight Dynamics Navigation and Safety," 12 in "Altimeter," and 6 in "Positional/Directional Sensing." Among these incidents, 100 are suspected to be due to GPS jamming and interference, leading to the loss of the main and auxiliary GPS units in some cases. What is alarming is the increasing trend of GPS interference—the majority of the aforementioned incidents took place since 2019. What is more, previously undisclosed U.S. Federal Aviation Administration data for a few months in 2017 and 2018 detail hundreds of aircraft losing GPS reception. On a single day in March 2018, 21 aircraft reported GPS problems to air traffic controllers near Los Angeles, CA, USA [2]. These and other incidents uncover the vulnerabilities of existing aircraft navigation systems, which are highly dependent on global navigation satellite system (GNSS) signals and their augmentation systems (e.g., ground-based augmentation systems and space-based augmentation systems) [3], [4]. There is an urgent need for complementary robust and accurate navigation systems to ensure aviation safety.

In 2019, the International Civil Aviation Organization issued a working paper titled "An Urgent Need to Address Harmful Interferences to GNSS," where it concluded that harmful radio-frequency (RF) interference to GNSS signals would prevent the full continuation of safety and efficiency benefits of GNSS-based services. Moreover, there was a call for supporting multidisciplinary development of alternative positioning, navigation, and timing strategy and solutions to complement the use of GNSS in aviation [5]. In 2021, the U.S. Department of Transportation released the "Complementary Positioning, Navigation, and Timing (PNT) and GPS Backup Technologies Demonstration Report" to Congress. The report concluded that, while there are suitable, mature, and commercially available technologies to back up or complement GPS, none of these systems alone can universally back up the PNT capabilities provided by GPS and its augmentations, necessitating a diverse universe of PNT technologies [6]. Moreover, in 2021, the National Institute of Standards and Technology issued a report on "Foundational PNT Profile: Applying the

The cellular SOPs produced remarkable navigation accuracy in all three flights, achieving a position RMSE of 10.53 m, 4.96 m, and 15.44 m, respectively.

Cybersecurity Framework for the Responsible Use of PNT Services," where it identified signals of opportunity (SOPs) and terrestrial RF sources (e.g., cellular) as a mitigation category that applies to the PNT profile [7].

Among terrestrial RF SOPs, cellular signals have shown tremendous potential as an alternative PNT source [8] because of their inherently desirable attributes:

- *Abundance*: Cellular base stations are abundant in most locales, with the number of base stations slated to increase dramatically with future cellular generations.
- *Geometric diversity*: Cellular base stations are placed in favorable geometric configurations by construction of the cellular infrastructure.
- *Frequency diversity*: In contrast to GNSS signals, cellular signals are transmitted at a wide range of frequencies, which makes them more difficult to be simultaneously jammed or spoofed.
- *High received power*: The received cellular carrier-to-noise ratio (CNR) is commonly tens of decibels higher than that of GNSS signals, even in deep urban canyons and indoor environments [9].
- *High bandwidth*: Downlink cellular signals can be up to 20 MHz [in 4G long-term evolution (LTE)] and even higher in future generations, which yields precise time-of-arrival estimates.
- *Free to use*: The cellular infrastructure is already operational; thus, with specialized receivers, navigation observables (pseudorange, carrier phase, and Doppler) can be extracted from the "always-on" transmitted signals.

Recent results have shown the ability of cellular SOPs to yield meter-level-accurate navigation on ground vehicles [10], [11] in urban environments and submeter-level-accurate navigation on unmanned aerial vehicles (UAVs) [12], [13]. Moreover, the robustness and availability of cellular SOPs have been demonstrated in a GPS-jammed environment [14].

Assessing cellular signals for aerial vehicles has been the subject of several studies recently [15]. These studies span radio channel modeling [16], [17]; evaluation of signal quality in terms of received signal power [18], [19], interference from cellular transmitters [20], [21], [22], and coverage and connectivity [23], [24], [25]; and standards recommendations [26], [27]. However, the majority of these studies focused on evaluating cellular signals for communication purposes with little attention to evaluating them for navigation purposes [28]. Moreover, they considered UAVs flying at low altitudes (up to 500 ft) and slow speeds (up to 50 km/h). A recent study revealed that cellular signals can be acquired and tracked at altitudes as high as 23,000 ft above ground level (AGL) and at horizontal distances of more than 100 km from cellular transmitters [29]. However, the potential of cellular SOPs for high-altitude aircraft navigation has not been thoroughly assessed. This article aims to perform the first assessment of cellular SOPs for aircraft navigation by addressing the following question: Can cellular SOPs be received and exploited at aircraft altitudes to produce a robust navigation solution?

To answer this question, an *unprecedented* aerial flight campaign was conducted in March 2020 by the Autonomous Systems Perception, Intelligence, and Navigation (ASPIN) Laboratory in collaboration with the U.S. Air Force (USAF) at the Edwards Air Force Base (AFB), CA, USA. The cellular software-defined radios (SDRs) of the ASPIN Laboratory were flown over on a USAF Beechcraft C-12 Huron, a fixed-wing aircraft, to collect ambient cellular signals. This unique dataset consists of combinations of flight runs over three different environments (rural, semiurban, and urban) with altitudes ranging up to 23,000 feet and a multitude of trajectories and maneuvers, including straight segments, banking turns, holding patterns, and ascending and descending teardrops performed by members of the USAF Test Pilot School. During these large-scale experiments, terabytes of samples of 3G code-division multiple access (CDMA) and 4G LTE signals were recorded under various conditions.

This article provides the first extensive demonstrations of their kind of utilizing cellular SOPs for navigation purposes on high-altitude aircraft. The aim of these demonstrations is to show that, should GNSS signals become unavailable or unreliable mid-flight, cellular SOPs could be used to produce a sustained and accurate navigation solution over trajectories spanning tens of kilometers.

To demonstrate the feasibility of aircraft navigation with cellular SOPs, three flights are performed in three different regions: 1) rural, 2) semiurban, and 3) urban. A multitude of flight trajectories and altitudes AGL was exercised in the three flights: 1) a 51-km trajectory of grid maneuvers with banking and straight segments at about 5,000 ft AGL, 2) a 57-km trajectory of a teardrop descent from 7,000 ft AGL down to touchdown at the runway, and 3) a 55-km trajectory of a holding pattern at about 15,000 ft AGL.

The aircraft's trajectory is estimated for each flight exclusively from cellular SOPs using an extended Kalman filter (EKF). The estimated aircraft trajectory is compared with the aircraft's onboard navigation system, which used a GPS-aided inertial navigation system (INS) and an

altimeter. The cellular SOPs produced remarkable navigation accuracy in all three flights, achieving a position root mean-squared error (RMSE) of 10.53 m, 4.96 m, and 15.44 m, respectively.

The rest of this article is organized as follows. The "Model Description" section describes the aircraft dynamics and cellular SOP measurement model. The "Navigation Framework" section formulates the EKF navigation framework. The "Experimental Setup and Flight Regions" section describes the experimental setup with which the aircraft was equipped and overviews the environments in which the flight campaigns took place. The "Aerial Navigation Results" section presents experimental aircraft navigation results exclusively with cellular signals. The "Conclusion" section gives concluding remarks.

ASPIN Laboratory's SDR, called the *Multichannel Adaptive Transceiver Information Extractor*, produces several types of navigation observables.

Model Description

This section describes the aircraft dynamics and cellular SOP measurement models used in the rest of the article.

Aircraft Dynamics Model

Depending on the aircraft's motion and sensor suite, different dynamic models can be used to describe its dynamics. The goal of this article is to assess the minimum performance of aircraft navigation with cellular SOPs exclusively. As such, a simple, yet effective continuous Wiener process acceleration model is employed, which upon discretization at a constant sampling interval T, is given by

$$\boldsymbol{x}_{\text{pva}}(k+1) = \mathbf{F}_{\text{pva}}\boldsymbol{x}_r(k) + \boldsymbol{w}_{\text{pva}}(k), \quad k = 0, 1, 2, \ldots$$
$$\mathbf{F}_{\text{pva}} = \begin{bmatrix} \mathbf{I}_{3\times3} & T\mathbf{I}_{3\times3} & \frac{T^2}{2}\mathbf{I}_{3\times3} \\ \mathbf{0}_{3\times3} & \mathbf{I}_{3\times3} & T\mathbf{I}_{3\times3} \\ \mathbf{0}_{3\times3} & \mathbf{0}_{3\times3} & \mathbf{I}_{3\times3} \end{bmatrix} \tag{1}$$

where $\boldsymbol{x}_{\text{pva}} \triangleq [\boldsymbol{r}_r^\intercal, \dot{\boldsymbol{r}}_r^\intercal, \ddot{\boldsymbol{r}}_r^\intercal]^\intercal$, $\boldsymbol{r}_r \triangleq [x_r, y_r, z_r]^\intercal$ is the 3D position of the aircraft expressed in a North-East-Down (NED) frame, and $\boldsymbol{w}_{\text{pva}}$ is a discrete-time zero-mean white noise sequence with covariance $\mathbf{Q}_{\text{pva}}$ given by

$$\mathbf{Q}_{\text{pva}} = \begin{bmatrix} \frac{T^5}{20} & \frac{T^4}{8} & \frac{T^3}{6} \\ \frac{T^4}{8} & \frac{T^3}{3} & \frac{T^2}{2} \\ \frac{T^3}{6} & \frac{T^2}{2} & T \end{bmatrix} \otimes \tilde{\mathbf{S}}_{\text{NED}}$$

where $\otimes$ denotes the Kronecker product, and $\tilde{\mathbf{S}}_{\text{NED}} \triangleq \text{diag}[\tilde{q}_N, \tilde{q}_E, \tilde{q}_D]$, where $\tilde{q}_N$, $\tilde{q}_E$, and $\tilde{q}_D$ are the NED jerk continuous-time noise power spectra, respectively. It should be noted that more complicated dynamic models can be used to describe the aircraft's dynamics, e.g., Singer acceleration, mean-adaptive acceleration, circular motion, curvilinear motion, and coordinated turn, among others [30]. Of course, if an INS is available, its measurements can be used to describe the aircraft's motion, while the INS is aided with cellular SOPs [31].

Clock Error Dynamics Model

Wireless standards require cellular base stations to be synchronized to within a few microseconds, which is order of magnitudes higher than the nanosecond requirements in GNSS. As such, the base station clock errors, which are dynamic and stochastic, must be accounted for in the navigation filter when navigating with cellular SOPs. A typical model for the dynamics of the clock error states is the so-called *two-state model*, composed of the clock bias δt and clock drift $\dot{\delta t}$, given by

$$\boldsymbol{x}_{\text{clk}}(k+1) = \mathbf{F}_{\text{clk}}\boldsymbol{x}_{\text{clk}}(k) + \boldsymbol{w}_{\text{clk}}(k) \tag{2}$$

where $\boldsymbol{w}_{\text{clk}}$ is a discrete-time zero-mean white noise sequence with covariance $\mathbf{Q}_{\text{clk}}$, and

$$\mathbf{F}_{\text{clk}} = \begin{bmatrix} 1 & T \\ 0 & 1 \end{bmatrix}, \quad \mathbf{Q}_{\text{clk}} = \begin{bmatrix} S_{\tilde{w}_{\delta t}} T + S_{\tilde{w}_{\dot{\delta t}}} \frac{T^3}{3} & S_{\tilde{w}_{\dot{\delta t}}} \frac{T^2}{2} \\ S_{\tilde{w}_{\dot{\delta t}}} \frac{T^2}{2} & S_{\tilde{w}_{\dot{\delta t}}} T \end{bmatrix}. \tag{3}$$

The power spectra $S_{\tilde{w}_{\delta t}}$ and $S_{\tilde{w}_{\dot{\delta t}}}$ are determined by the quality of the oscillator from which the clock signal is derived [32].

SOP Measurement Model

ASPIN Laboratory's SDR, called the *Multichannel Adaptive Transceiver Information Extractor* (*MATRIX*), produces several types of navigation observables. To get the highest possible precision, carrier phase observables are exploited for navigation, which after some manipulations can be modeled as [14]

$$z_n(k) = \| \boldsymbol{r}_r(k) - \boldsymbol{r}_{s_n} \|_2 + c\delta t_n(k) + v_n(k), \quad n = 1, 2, \ldots, N \tag{4}$$

where $\boldsymbol{r}_{s_n}$ is the nth cellular base station's 3D position vector; c is the speed of light; δt_n is the overall clock error in the nth carrier phase measurement, which combines the effect of receiver and base station clock biases and the initial carrier phase ambiguity; N is the total number of available base

stations; and $v_n(k)$ is the measurement noise, which is modeled as a discrete-time zero-mean white Gaussian sequence with variance $\sigma_n^2(k)$. The measurement noise variance can be modeled as a function of the CNR [33], [34].

Altimeter Measurement Model

Since cellular base stations appear to have similar altitudes for a high-flying aircraft, their vertical dilution of precision (VDOP) will be very large. To circumvent this issue, the altimeter data z_{alt} derived from the aircraft's onboard navigation system is used in addition to the cellular carrier phase measurements in the measurement-update step in the EKF.

Navigation Framework

This section formulates the EKF navigation framework based on the models presented in the "Model Description" section.

EKF Model

Let $\boldsymbol{x} \triangleq [\boldsymbol{x}_{\text{pv}}^{\mathsf{T}}, \boldsymbol{x}_{\text{clk}_1}^{\mathsf{T}}, \ldots, \boldsymbol{x}_{\text{clk}_N}^{\mathsf{T}}]^{\mathsf{T}}$ denote the state to be estimated, where $\boldsymbol{x}_{\text{clk}_n} \triangleq [c\delta t_n, c\dot{\delta} t_n]^{\mathsf{T}}$. Using (1) and (2), one can write the dynamics of $\boldsymbol{x}$ as

$$\boldsymbol{x}(k+1) = \mathbf{F}\boldsymbol{x}(k) + \boldsymbol{w}(k) \tag{5}$$

where $\mathbf{F} \triangleq \text{diag}[\mathbf{F}_{\text{pva}}, \mathbf{F}_{\text{clk}}, \ldots, \mathbf{F}_{\text{clk}}]$ and $\boldsymbol{w}(k)$ is the overall process noise vector, which is a zero-mean white sequence with covariance $\mathbf{Q} \triangleq \text{diag}[\mathbf{Q}_{\text{pva}}, \bar{\mathbf{Q}}_{\text{clk}}]$, and

$$\bar{\mathbf{Q}}_{\text{clk}} \triangleq \begin{bmatrix} \mathbf{Q}_{\text{clk}_r} + \mathbf{Q}_{\text{clk}_{s1}} & \mathbf{Q}_{\text{clk}_r} & \cdots & \mathbf{Q}_{\text{clk}_r} \\ \mathbf{Q}_{\text{clk}_r} & \mathbf{Q}_{\text{clk}_r} + \mathbf{Q}_{\text{clk}_{s2}} & \cdots & \mathbf{Q}_{\text{clk}_r} \\ \vdots & \vdots & \ddots & \vdots \\ \mathbf{Q}_{\text{clk}_r} & \mathbf{Q}_{\text{clk}_r} & \cdots & \mathbf{Q}_{\text{clk}_r} + \mathbf{Q}_{\text{clk}_{s_N}} \end{bmatrix}$$

where $\mathbf{Q}_{\text{clk}_r}$ and $\{\mathbf{Q}_{\text{clk}_{sn}}\}_{n=1}^{N}$ have the same form as in (3), except that $S_{\tilde{w}_{\delta t}}$ and $S_{\tilde{w}_{\dot{\delta} t}}$ are replaced with the receiver and nth base station's clock process noise spectra, respectively. Note that the cross correlations in $\bar{\mathbf{Q}}_{\text{clk}}$ come from combining the effect of the receiver and cellular base station clocks in the same state. Since the receiver clock bias is common to all clock states, the cross correlations in $\bar{\mathbf{Q}}_{\text{clk}}$ will be the receiver clock's process noise covariance [35].

The measurement vector defined by $\boldsymbol{z}(k) \triangleq [z_{\text{alt}}(k), z_1(k), \ldots, z_N(k)]^{\mathsf{T}}$ is used to estimate $\boldsymbol{x}$ in the EKF. In vector form, the measurement equation is given by

$$\boldsymbol{z}(k) = \boldsymbol{h}[\boldsymbol{x}(k)] + \boldsymbol{v}(k) \tag{6}$$

where $\boldsymbol{h}[\boldsymbol{x}(k)]$ is a vector-valued function defined as $\boldsymbol{h}[\boldsymbol{x}(k)] \triangleq [h_{\text{alt}}[\boldsymbol{x}(k)], h_1[\boldsymbol{x}(k)], \ldots, h_N[\boldsymbol{x}(k)]]^{\mathsf{T}}$ with $h_{\text{alt}}[\boldsymbol{x}(k)] = z_r(k) + v_{\text{alt}}(k)$, $h_n[\boldsymbol{x}(k)] \triangleq \| \boldsymbol{r}_r(k) - \boldsymbol{r}_{s_n} \|_2 + c\delta t_n(k)$, and $\boldsymbol{v}(k) \triangleq [v_{\text{alt}}(k), v_1(k), \ldots, v_N(k)]^{\mathsf{T}}$ is the measurement noise vector, which is modeled as a zero-mean white Gaussian random vector with covariance $\mathbf{R}(k) \triangleq \text{diag}[\sigma_{\text{alt}}^2(k), \sigma_1^2(k), \ldots, \sigma_N^2(k)]$.

An EKF is implemented given the dynamics and measurement models in (5) and (6) to produce an estimate of $\boldsymbol{x}(k)$ using all measurements up to time step k, denoted by $\hat{\boldsymbol{x}}(k|k)$, and an associated estimation error covariance denoted by $\mathbf{P}(k|k)$. The EKF is initialized from two successive position priors according to the framework discussed in [35]. The EKF process and measurement noise covariances are described in the next section.

EKF Settings

The measurement rate was $T = 0.08/3$ s; the jerk process noise spectra were chosen to be $\tilde{q}_N = 18\ \text{m}^2/\text{s}^5$, $\tilde{q}_E = 18\ \text{m}^2/\text{s}^5$, and $\tilde{q}_D = 0.5\ \text{m}^2/\text{s}^5$; and the receiver and base station clock process noise covariance matrices were chosen to be

$$\mathbf{Q}_{\text{clk},r} = \begin{bmatrix} 9.57 \times 10^{-5} & 2.52 \times 10^{-8} \\ 2.52 \times 10^{-8} & 1.89 \times 10^{-6} \end{bmatrix} \tag{7}$$

$$\mathbf{Q}_{\text{clk},s_n} = \begin{bmatrix} 3.11 \times 10^{-7} & 2.52 \times 10^{-11} \\ 2.52 \times 10^{-11} & 1.89 \times 10^{-9} \end{bmatrix}. \tag{8}$$

These clock process noise covariance matrices assumed the receiver to be equipped with a typical temperature-compensated crystal oscillator (TCXO), while the cellular base stations are equipped with a typical oven-controlled crystal oscillator (OCXO) [8].

The altimeter measurement error variance $\sigma_{\text{alt}}^2(k)$ was assumed to be $5\ \text{m}^2$. The cellular measurement noise variances were calculated as a function of the CNR and receiver parameters, as discussed in [33] and [34]. The range of values taken by the measurement noise variances is explicitly stated for each region in the "Aerial Navigation Results" section.

Experimental Setup and Flight Regions

This section overviews the experimental setup used for data collection and processing. It also describes the flight regions.

Hardware and Software Setup

The C-12 aircraft was equipped with a universal software radio peripheral (USRP) with consumer-grade cellular antennas to sample three cellular bands and store the samples on a desktop computer for offline processing. The stored samples were postprocessed with the 3G and 4G cellular modules of MATRIX. The SDR produces navigation observables: Doppler frequency, carrier phase, and pseudorange, along with corresponding CNRs. The hardware setup is shown in Figure 1.

The aircraft's ground-truth trajectory was taken from the C-12's onboard Honeywell H764-ACE EGI INS/GPS, which provided time–space–position information at a 1-Hz data rate. The accuracy specifications are tabulated in Table 1.

Flight Regions

Three flights are reported in this article, each of which took place in one of three regions: 1) Region A: a rural region in

Edwards AFB, CA; 2) Region B: a semiurban region in Palmdale, CA; and 3) Region C: an urban region in Riverside, CA. Different maneuvers were planned over the three regions to test several aspects of aircraft navigation with cellular SOPs.

Figure 2 shows the regions in which the experiments were performed as well as the aircraft trajectory for each flight. The 3G base transceiver stations (BTSs) and 4G eNodeBs were mapped via the method described in [36]. The mapped towers were cross-checked via Google Earth and online databases and are shown in Figure 2. This article investigates the potential of cellular SOPs for navigation; therefore, mapping the SOPs will not be discussed.

Aerial Navigation Results

This section presents experimental results demonstrating high-altitude aircraft navigation using the framework discussed in the "Model Description" section in the three regions shown in Figure 2.

Aerial Navigation in Region A

The test trajectory in Region A consisted of 1) a 24-km straight segment, followed by 2) a 270° banking turn of length 18 km, and 3) a final 9-km straight segment. The total distance traveled by the aircraft was more than 51 km, completed in 9 min. The aircraft maintained an altitude of approximately 5,000 ft AGL throughout the trajectory. During this flight, three RF channels were sampled at 1) 881.52 MHz, which is a 3G channel allocated for the U.S. cellular provider Verizon Wireless; 2) 731.5 MHz, a 4G LTE channel allocated for T-Mobile; and 3) 751 MHz, also a 4G LTE channel allocated for Verizon. A total of 11 cellular SOPs were heard during the experiment: six 3G BTSs and five 4G eNodeBs. The 11 cellular SOPs were acquired at different times and tracked for different durations based on signal quality. Figure 3(a)–(c) shows the time history of the 1) measured CNRs, 2) pseudorange measurements, and 3) pseudorange error (pseudorange minus the true range) for all 11 cellular SOPs, respectively. One can see from Figure 3(c) that

Table 1. Honeywell H764-ACE EGI accuracy.

Metric	Blended INS/GPS Accuracy
Position	5 m, spherical error probable
Velocity	0.01 m/s
Heading	0.015°
Pitch/Roll	0.01°

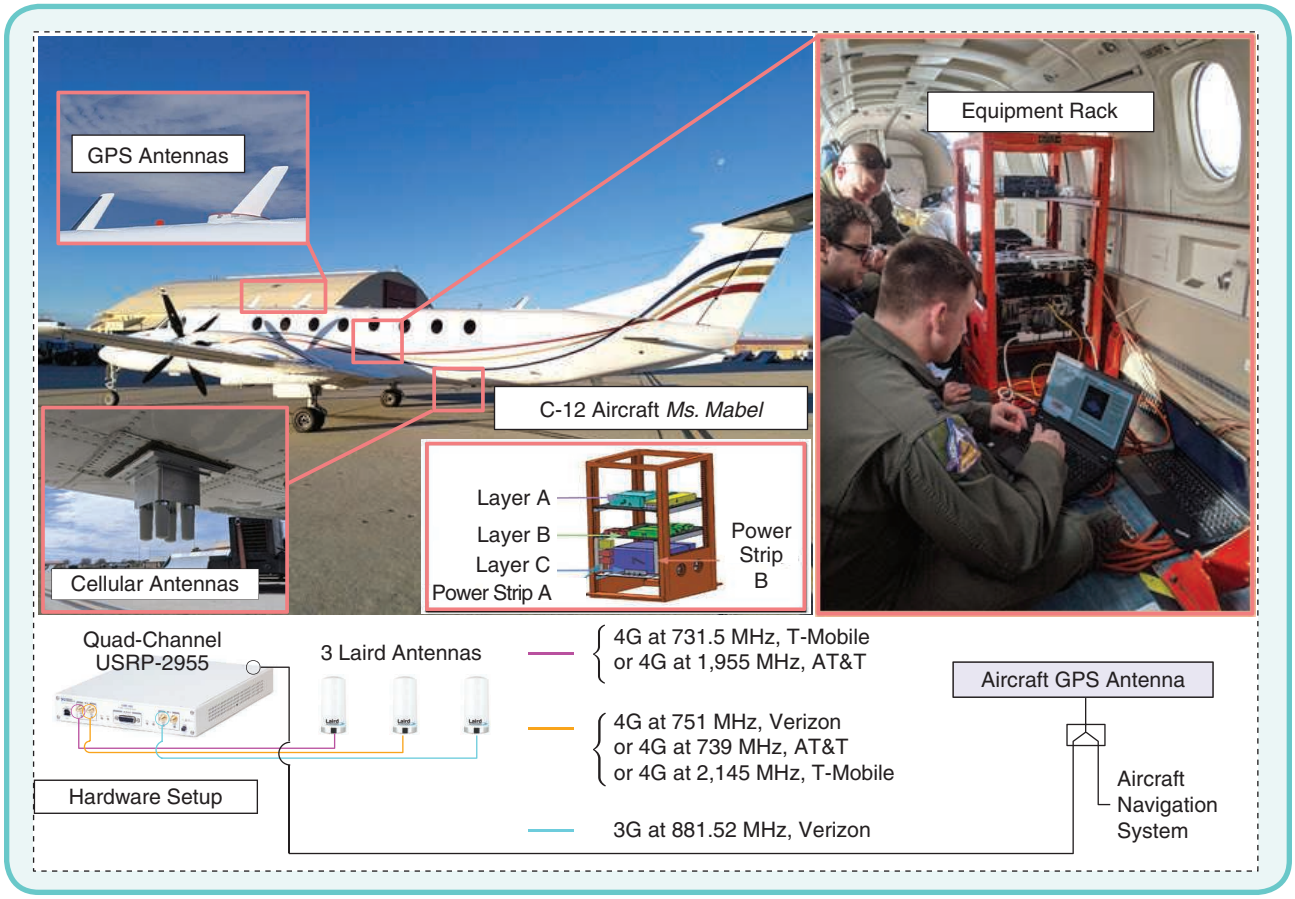

FIG 1 Hardware setup with which the C-12 aircraft was equipped.

It is suspected that the aircraft's wings and body block or severely attenuate some of the signals during banking, causing loss of tracking.

pseudorange tracking is lost for some of the cellular SOPs at or around 300 s, which is when the aircraft starts banking to perform the 270° turn. In addition to the high dynamics of the banking turn, it is suspected that the aircraft's wings and body block or severely attenuate some of the signals during banking, causing loss of tracking. Using the expressions of the measurement noise variances as a function of the CNR and receiver parameters in [33] and [34], $\sigma_n(k)$ was found to vary between 1.44 and 9.47 m.

Next, the state vector $\boldsymbol{x}$ of the aircraft was estimated using the carrier phase measurements obtained from the cellular SOP receivers via the EKF discussed in the "EKF Model" section. The total position RMSE was calculated to be 10.5 m over the 51-km trajectory, traversed in 9 min. Figure 4 shows the aircraft's true and estimated trajectories. Figure 5 shows the EKF estimation error plots and corresponding sigma bounds for the aircraft's position and velocity states. It is important to note that the position error in the EKF is the largest during the turn. This is due to 1) the measurement errors due to the high dynamics of the banking turn, which severely stressed the tracking loops, and 2) the mismatch in the dynamics model assumed in the EKF since a 270° banking turn has significantly different dynamics than the assumed continuous Wiener process acceleration model. However, as mentioned earlier, the purpose of this study is to highlight the minimum performance that can be achieved with cellular SOPs. It is important to note that the average distance between the aircraft and the BTSs or eNodeBs was around 30 km over the entire trajectory, with eNodeB 4 being tracked at a 100-km distance in the first part of the trajectory.

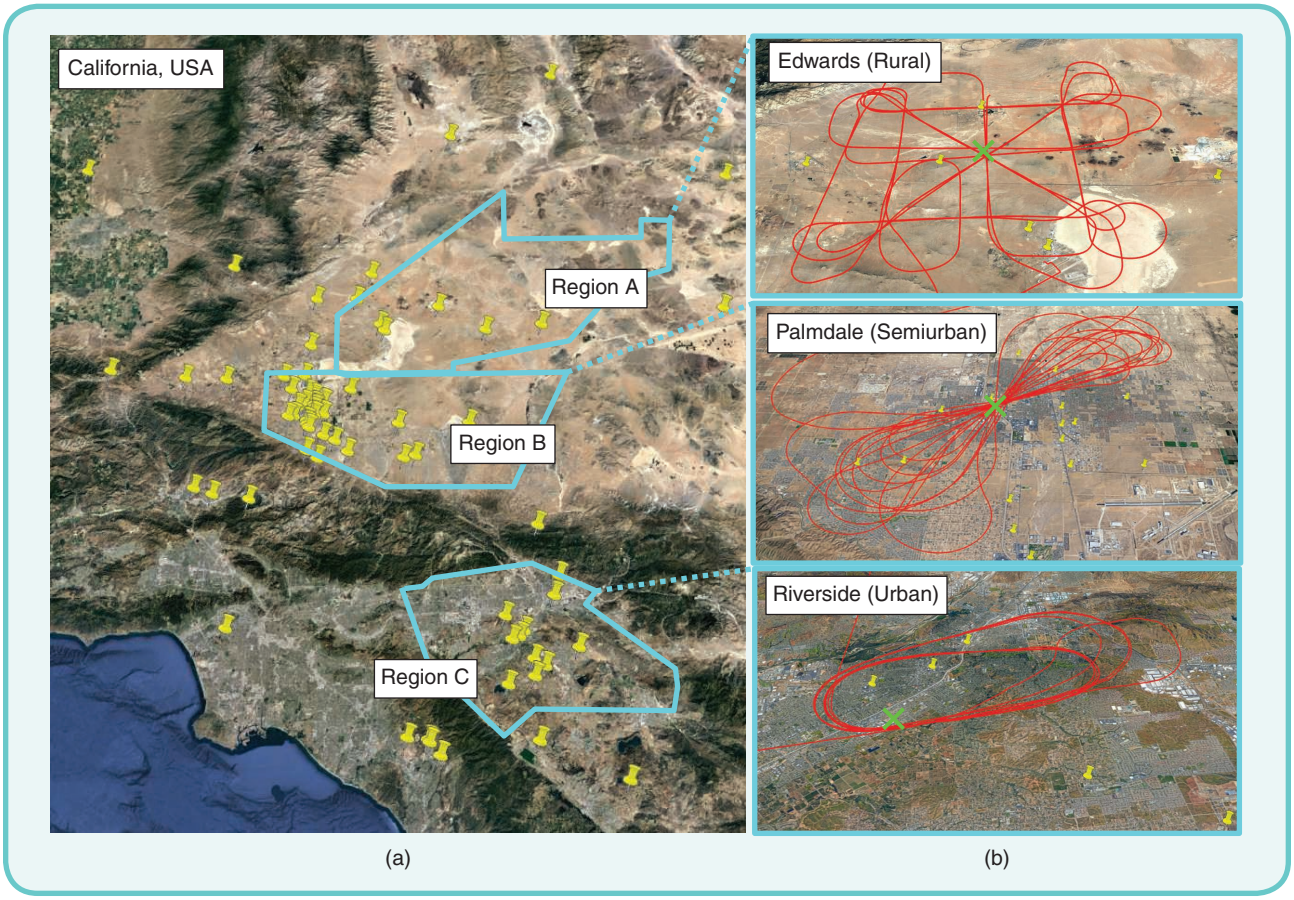

FIG 2 (a) Regions A, B, and C in which the flight campaigns took place. The yellow pins represent 3G and 4G cellular towers that were mapped and analyzed in this study. (b) The aircraft trajectories in all regions (shown in red). Geographic points of interest in each region, shown by green crosses, were chosen according to the designed trajectories.

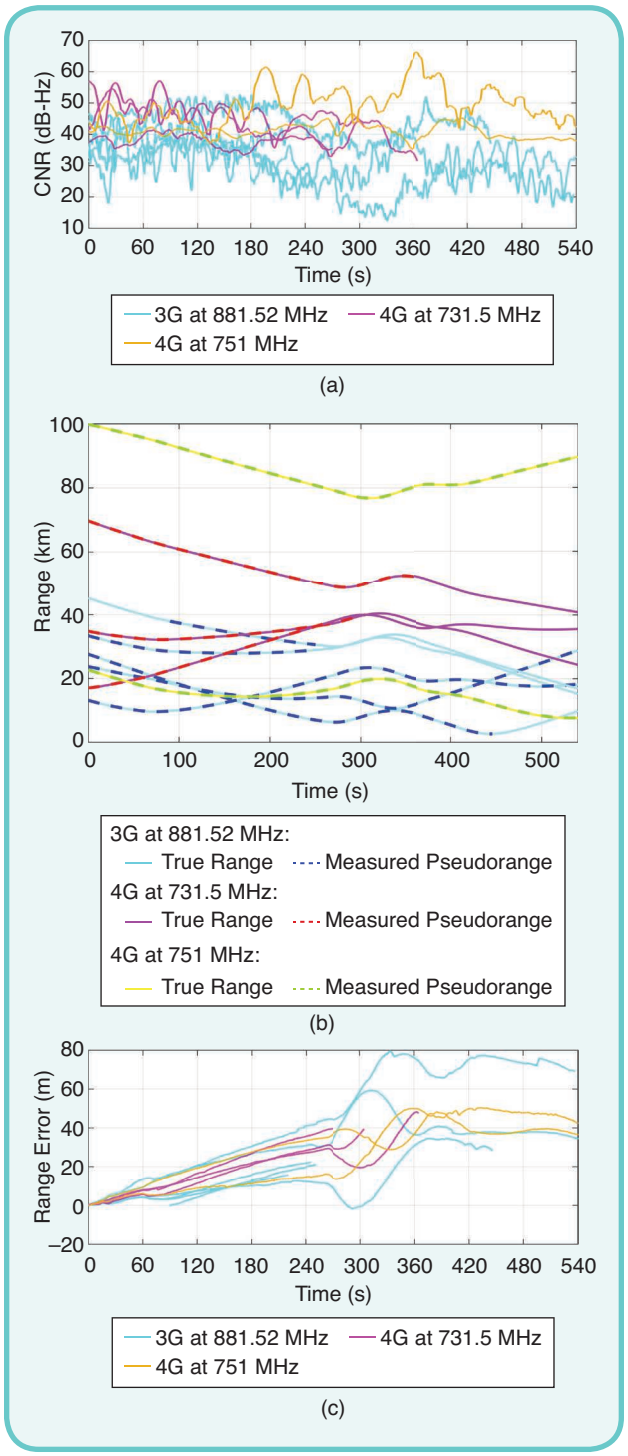

FIG 3 (a) Time history of the CNRs for all of the base stations used to compute the navigation solution in Region A. (b) Time history of the pseudoranges estimated by the cellular SOP receivers and the corresponding true range in Region A. The initial values of the pseudoranges and ranges were subtracted out for ease of comparison. (c) Time history of the pseudorange error (pseudorange minus the true range) for all cellular SOPs in Region A. The error is driven by a common term, which is the receiver's clock bias. The errors increase significantly at around 300 s, which is when the turn starts. The high dynamics of a banking turn inject stress on the tracking loops. The initial values of the pseudorange errors were subtracted out for ease of comparison.

Aerial Navigation in Region B

The test trajectory in Region B consisted of 1) an approach to General William J. Fox Airfield, followed by 2) a touch and go. The total distance traveled by the aircraft was more than 57 km completed in 11 min. The aircraft descended from an

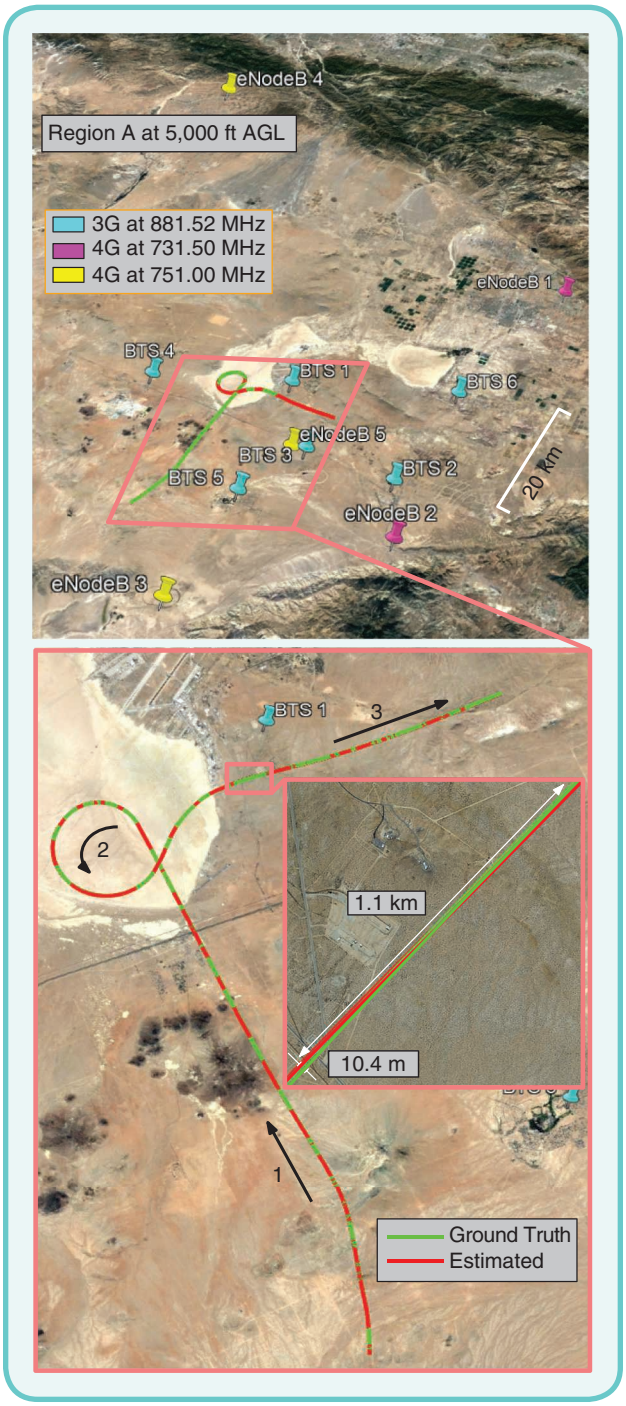

FIG 4 Experimental layout and results in Region A showing BTS and eNodeB positions, true aircraft trajectory, and aircraft trajectory estimated exclusively using cellular SOPs. The aircraft traversed a total distance of 51 km in 9 min during the experiment. The position RMSE over the entire trajectory was found to be 10.5 m.

altitude of 7,000 ft AGL. During this flight, three RF channels were sampled at 1) 881.52 MHz, which is a 3G channel allocated for the U.S. cellular provider Verizon Wireless; 2) 731.5 MHz, a 4G LTE channel allocated for T-Mobile; and 3) 739 MHz, also a 4G LTE channel allocated for AT&T. A total of 14 cellular SOPs were heard during the experiment: nine 3G BTSs and five 4G eNodeBs. The 14 cellular SOPs were acquired at different times and tracked for different durations based on signal quality. Figure 6(a)–(c) shows the time history of 1) measured CNRs, 2) pseudorange measurements, and 3) pseudorange error (pseudorange minus the true range) for all 14 cellular SOPs, respectively. Using the expressions of the measurement noise variances as a function of the CNR and receiver parameters in [33] and [34], $\sigma_n(k)$ was found to vary between 1.3 to 4.43 m.

Next, the state vector $\boldsymbol{x}$ of the aircraft was estimated using the carrier phase measurements obtained from the cellular SOP receivers via the EKF discussed in the "EKF Model" section. The total position RMSE was calculated to be 4.95 m over the 57-km trajectory, traversed in 11 min. Figure 7 shows the aircraft's true and estimated trajectories. Figure 8 shows the EKF estimation error plots and corresponding sigma bounds for the aircraft's position and velocity states. It is important to note that the aircraft's position estimate on touchdown is less than 3 m away from the true position and is well within the runway. In addition, the geometric diversity becomes poor after the sixth minute as the aircraft is flying on one side of the SOPs. This explains the increasing sigma bounds in Figure 8.

Aerial Navigation in Region C

The test trajectory in Region C consisted of a holding pattern over Riverside Municipal Airport. The total distance traveled by the aircraft was more than 55 km, completed in 8.5 min. The aircraft maintained an altitude of approximately 15,000 ft AGL throughout the trajectory. During this flight, two RF channels were sampled at 1) 881.52 MHz, which is a 3G channel allocated for the U.S. cellular provider Verizon Wireless; 2) 1,955 MHz, a 4G LTE channel allocated for AT&T; and 3) 2,145 MHz, a 4G LTE channel allocated for T-Mobile. A total of 11 cellular SOPs were heard during the experiment: seven 3G BTSs and four 4G eNodeBs. The 11 cellular SOPs were acquired at different times and tracked for different durations based on signal quality. Figure 9(a)–(c) shows the time history of 1) measured CNRs, 2) pseudorange measurements, and 3) pseudorange error (pseudorange minus the true range), for all 9 cellular SOPs, respectively. Similar to the first flight, one can see from Figure 9(c) that pseudorange tracking is lost for some

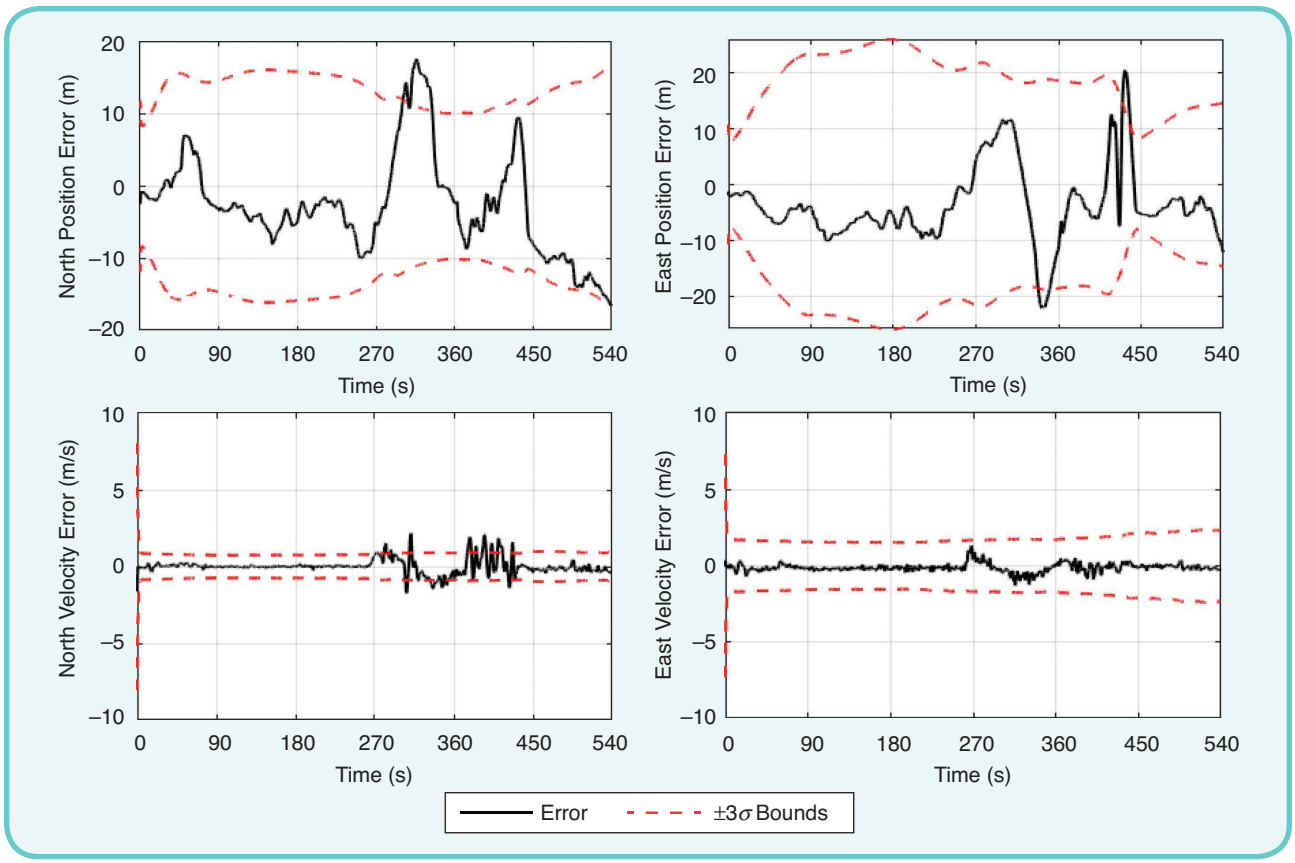

FIG 5 EKF plots showing the time history of the position and velocity errors in Region A as well as the $\pm 3\sigma$ bounds. As expected, the EKF performs poorly in the second leg, where the mismatch between the true aircraft dynamics and the assumed EKF model is highest.

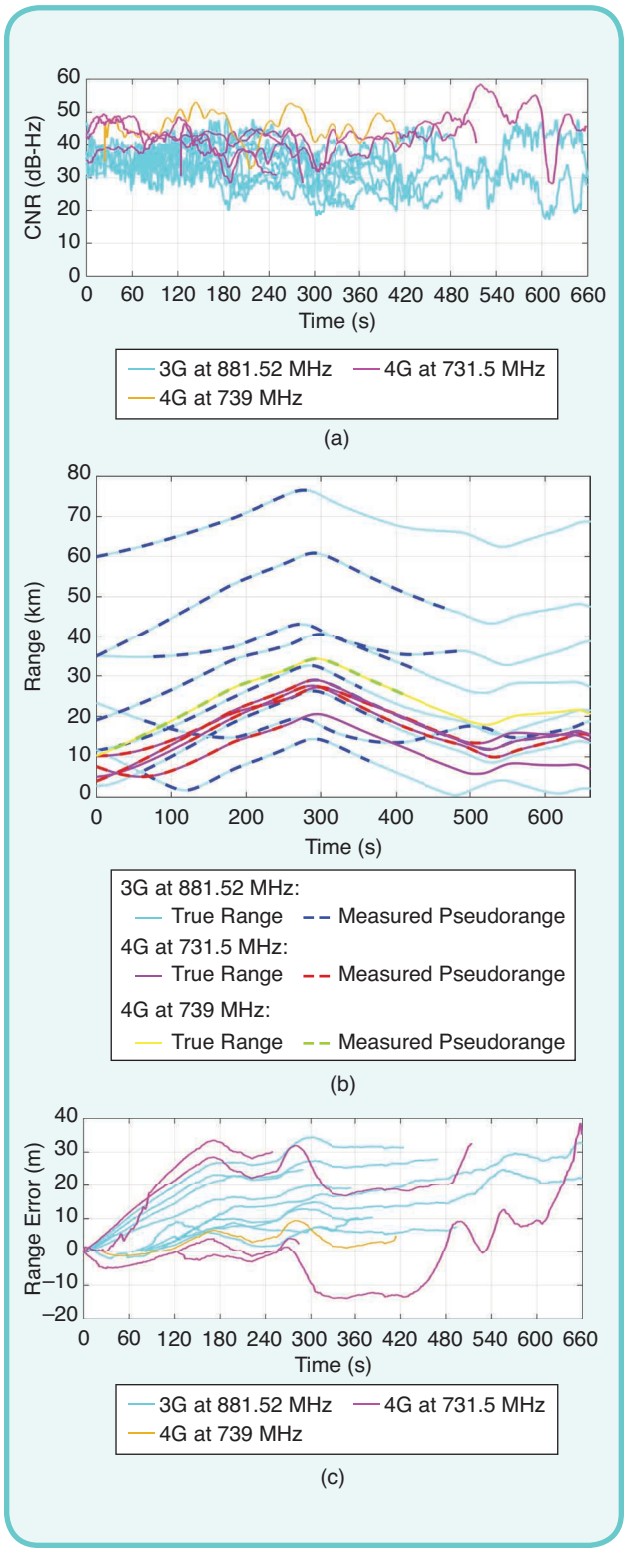

FIG 6 (a) Time history of the CNRs for all of the base stations used to compute the navigation solution in Region B. (b) Time history of the pseudoranges estimated by the cellular SOP receivers and the corresponding true range in Region B. The initial values of the pseudoranges and ranges were subtracted out for ease of comparison. (c) Time history of the pseudorange error (pseudorange minus the true range) for all cellular SOPs in Region B.

of the cellular SOPs when the aircraft starts banking to perform the turns in the holding pattern. Using the expressions of the measurement noise variances as a function of the CNR and receiver parameters in [33] and [34], $\sigma_n(k)$ was found to vary between 1.73 and 5.69 m.

Next, the state vector $\boldsymbol{x}$ of the aircraft was estimated using the carrier phase measurements obtained from the cellular SOP receivers via the EKF discussed in the "EKF Model" section. The total position RMSE was calculated to be 15.44 m over the 55-km trajectory, traversed in 8.5 min. Figure 10 shows the aircraft's true and estimated trajectories. Figure 11 shows the EKF estimation error plots and corresponding sigma

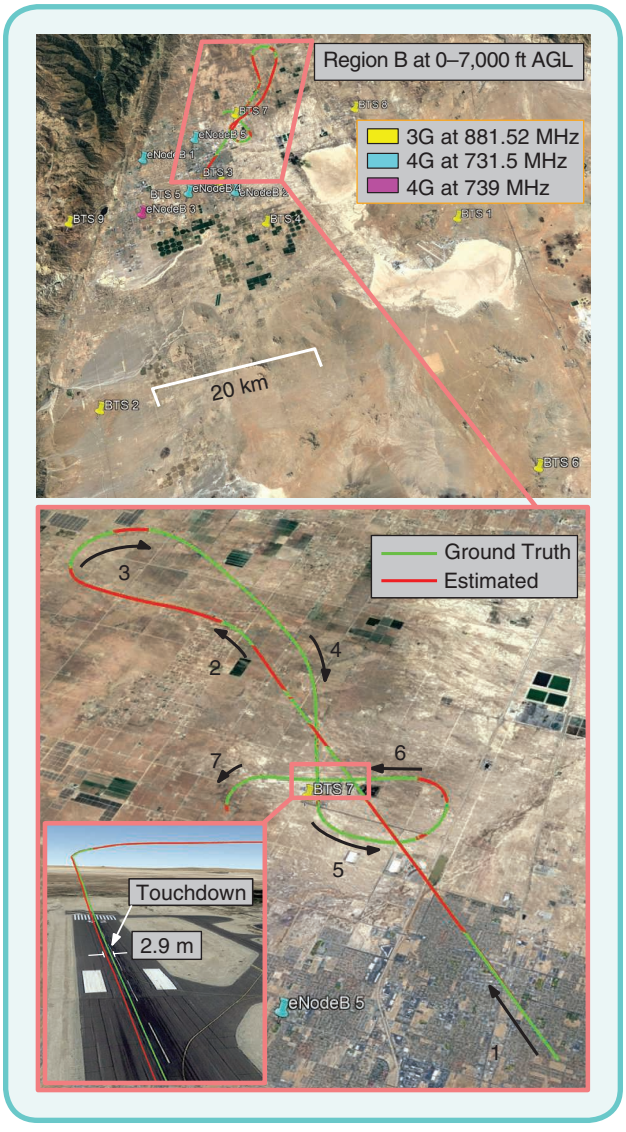

FIG 7 Experimental layout and results in Region B showing BTS and eNodeB positions, true aircraft trajectory, and aircraft trajectory estimated exclusively using cellular SOPs. The aircraft traversed a total distance of 57 km in 11 min during the experiment. The position RMSE over the entire trajectory was found to be 4.96 m. Note that the position estimate on touchdown is less than 3 m away from the true aircraft position and is well within the runway.

The achieved results unveiled the remarkable potential of utilizing cellular SOPs for sustained accurate high-altitude aircraft navigation.

bounds for the aircraft's position and velocity states. As expected, the measurement errors and the mismatch in the dynamics model assumed in the EKF are more severe during the turns.

Discussion

The navigation performance in all three regions is summarized in Table 2.

The achieved results unveiled the remarkable potential of utilizing cellular SOPs for sustained accurate high-altitude aircraft navigation. The results presented herein, although promising, can be further improved upon in several ways. The following are key takeaways and design considerations for reliable aircraft navigation with cellular SOPs:

- *Accounting for the aircraft dynamical model mismatch*: Aircraft, such as the C-12, can perform a variety of highly dynamic maneuvers. The dynamics model employed in the EKF in this study did not perfectly capture the aircraft dynamics throughout its trajectory, leading to an increased estimation error due to the mismatch between the actual aircraft's dynamics and the dynamical model assumed by the EKF. This mismatch can be mitigated by using appropriate dynamical models for fixed-wing aircraft or more elaborate dynamical models (e.g., Wiener process acceleration, Singer acceleration, mean-adaptive acceleration, a semi-Markov jump process, circular motion, curvilinear motion, and coordinated turns, among others [30]) coupled with adaptive estimation techniques [37], [38], [39], [40], [41], [42]. Alternatively, if access to raw inertial measurement unit (IMU) data is available, a kinematic model with IMU measurements can be used as is the case with most INS-aiding techniques [10], [31].
- *Accounting for statistical model mismatch*: The aircraft's process noise covariance assumed by the EKF's dynamical model was found via offline tuning and by

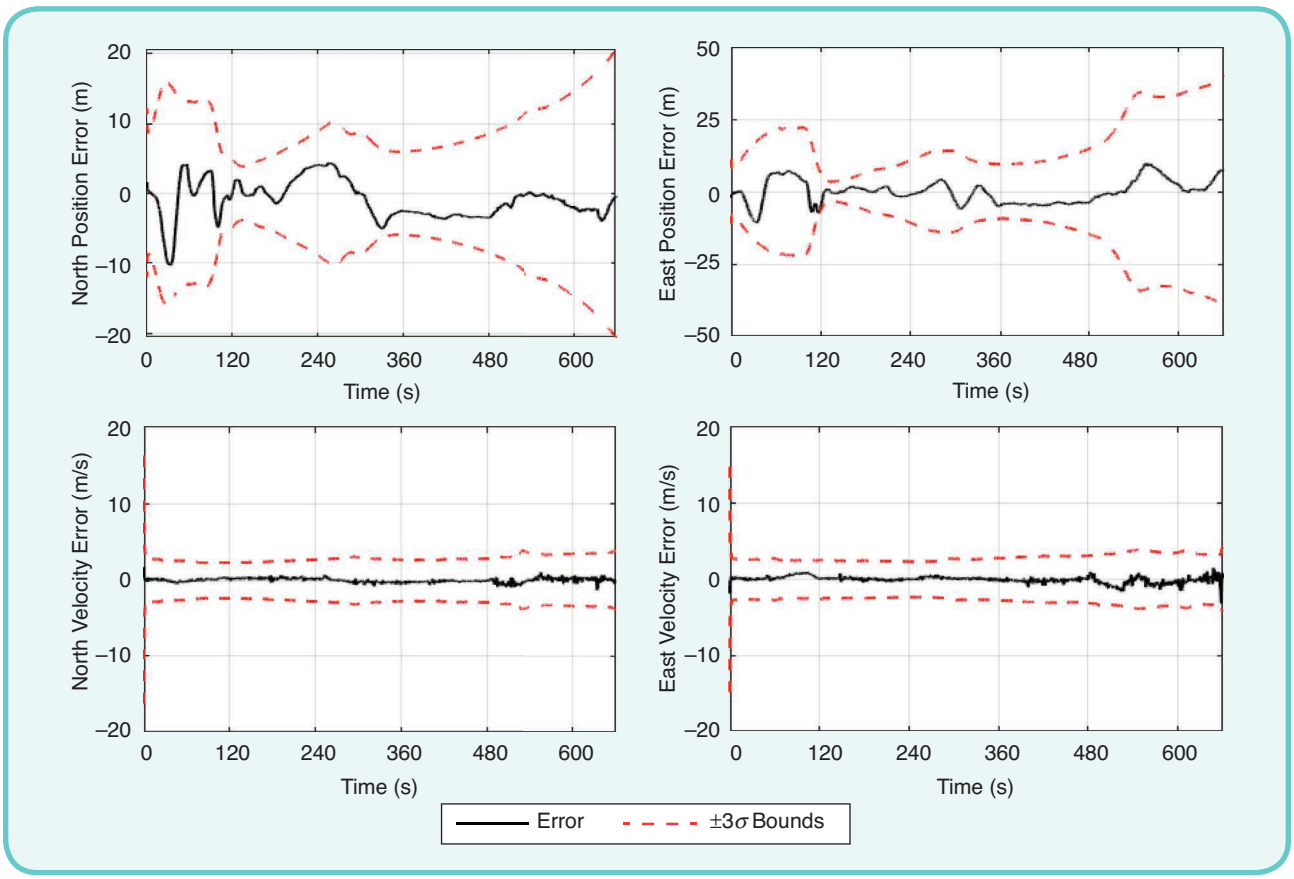

FIG 8 EKF plots showing the time history of the position and velocity errors in Region B as well as the $\pm 3\sigma$ bounds.

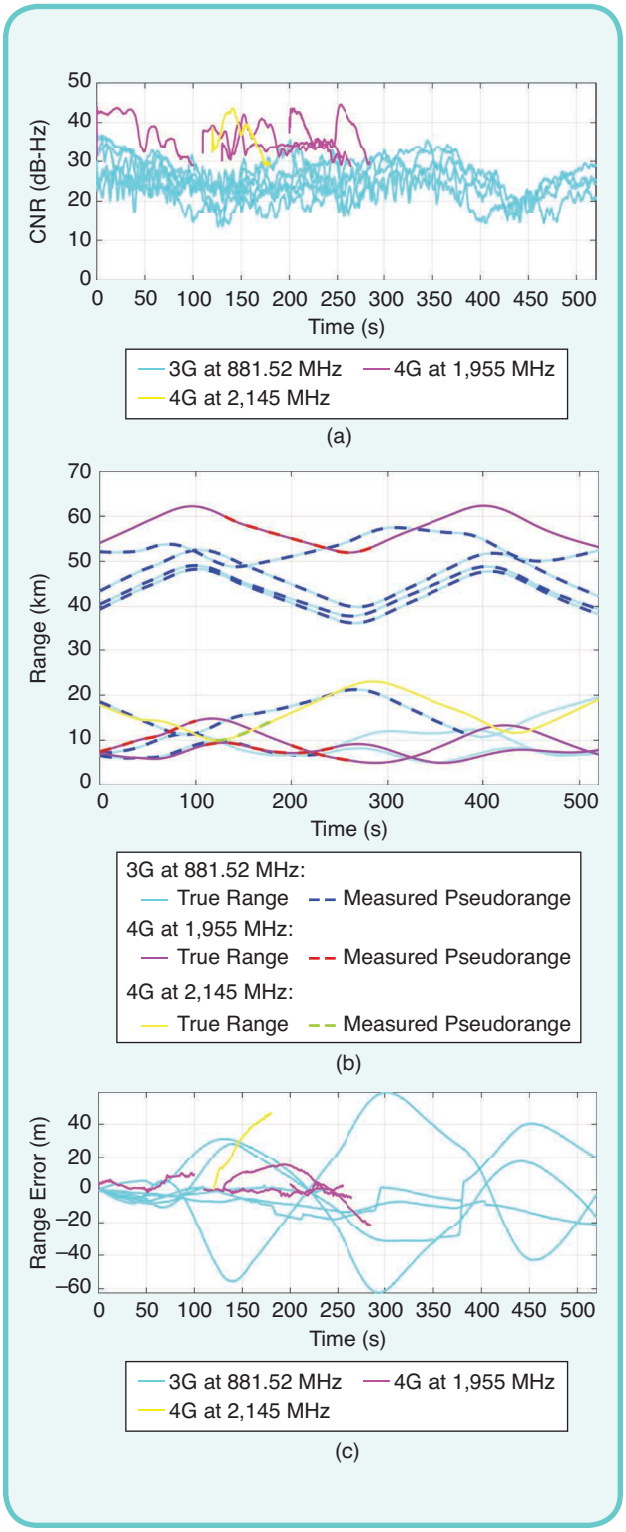

FIG 9 (a) Time history of the CNRs for all of the base stations used to compute the navigation solution in Region C. (b) Time history of the pseudoranges estimated by the cellular SOP receivers and the corresponding true range in Region C. The initial values of the pseudoranges and ranges were subtracted out for ease of comparison. (c) Time history of the pseudorange error (pseudorange minus the true range) for all cellular SOPs in Region C. The error is driven by a common term, which is the receiver's clock bias.

analyzing the aircraft's maneuvers from ground-truth data. In addition, the process noise covariances of the aircraft's receiver clock were set at typical TCXO values, and the cellular SOP transmitter clocks were set at typical OCXO values. While these values represent good approximations for the aircraft's receiver clock quality as well as the quality of typical cellular SOP transmitters, mismatches between the assumed values and the actual values can be mitigated via adaptive estimation techniques [43], [44], [45], which would improve

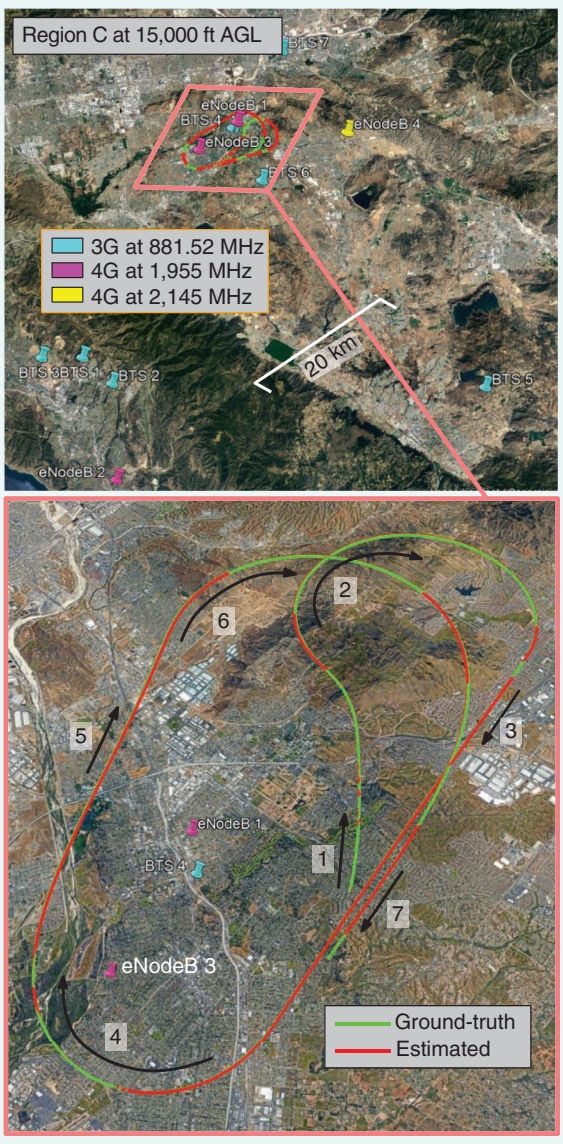

FIG 10 Experimental layout and results in Region C showing BTS and eNodeB positions, true aircraft trajectory, and aircraft trajectory estimated exclusively using cellular SOPs. The aircraft traversed a total distance of 55 km in 8.5 min during the experiment. The position RMSE over the entire trajectory was found to be 15.44 m.

the estimation performance. Adaptive estimation techniques would also mitigate the errors arising from mismatches between the actual measurement noise variances and calculated measurement noise variances.

- *Vertical dilution of precision*: At high altitudes, there is very little vertical diversity with respect to terrestrial cellular towers. As such, the aircraft's cellular-based navigation solution VDOP will be large. Nevertheless, the aircraft's vertical position can still be estimated from the pseudoranges extracted from cellular towers, albeit with less accuracy compared to the results presented in this article, which fused altimeter-based measurements.
- *Mapping cellular SOPs*: This article assumed cellular SOPs to be mapped a priori. This was achieved via a mapping campaign according to the method described in [36]. Nevertheless, such an assumption can be relaxed via the radio simultaneous localization and mapping framework, which maps the unknown SOPs simultaneously with localizing the aircraft [14], [31].

Table 2. Navigation performance with cellular signals.

Metric	Region A	Region B	Region C
Cellular towers {3G,4G}	{6,5}	{9,5}	{7,4}
Cellular frequencies (MHz)	881.52	881.52	881.52
	731.5	731.5	1,955
	751	739	2,145
Flight duration (min)	9	11	8.5
Flight length (km)	51	57	55
Altitude AGL (ft)	5,000	0–7,000	15,000
Position RMSE (m)	10.53	4.96	11.67
Velocity RMSE (m/s)	0.58	0.5	0.71
Maximum position error (m)	22.67	15.04	25.89
Maximum velocity error (m/s)	2.29	3.19	3.94

Conclusion

This article demonstrated robust high-altitude aircraft navigation with 3G CDMA and 4G LTE cellular SOPs. An EKF was used to fuse cellular carrier phase measurements to estimate the aircraft's position, velocity, and time. The EKF utilized a simple, yet effective continuous Wiener process acceleration model to describe the aircraft dynamics. A multitude of flight trajectories and altitudes AGL was exercised in the three flights: 1) a 51-km trajectory of grid maneuvers with banking and straight segments at about

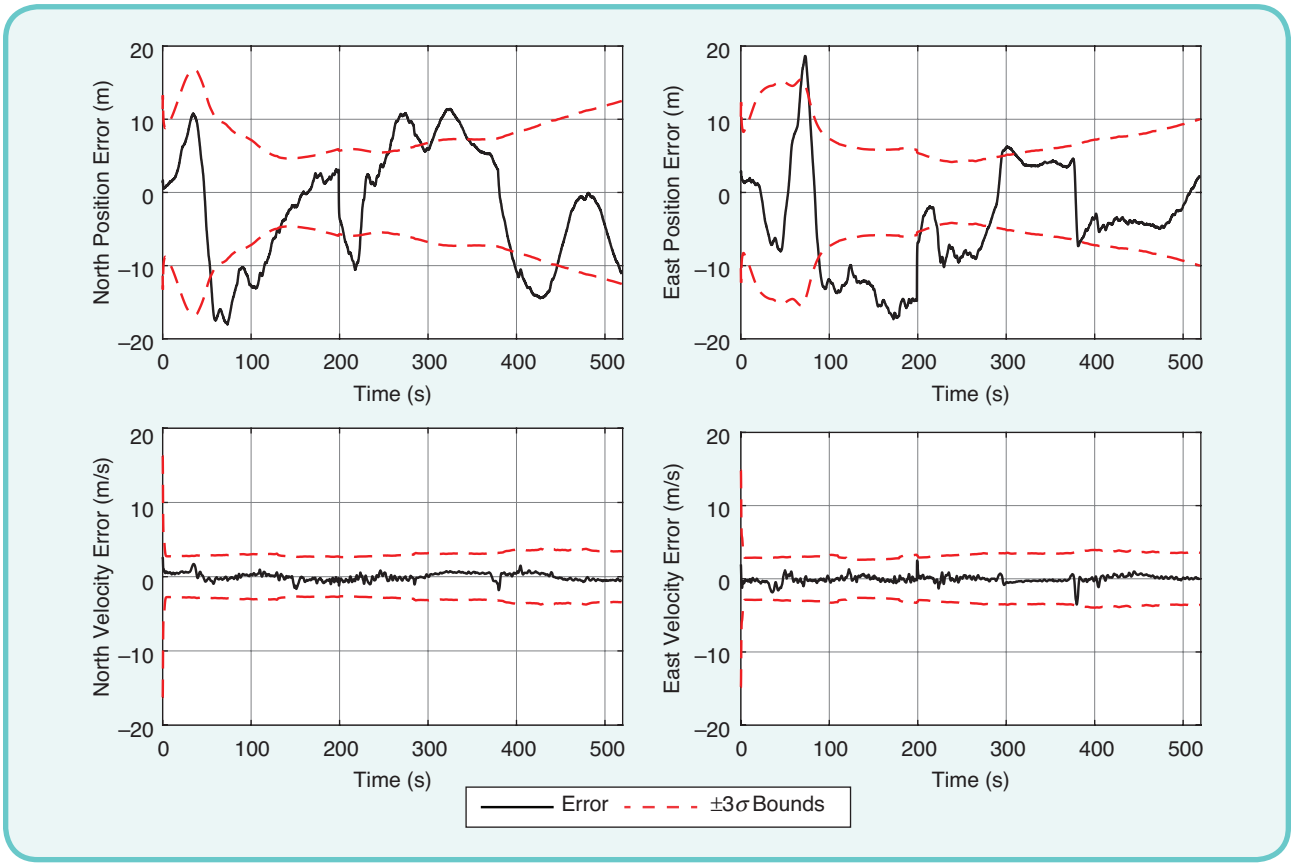

FIG 11 EKF plots showing the time history of the position and velocity errors in Region C as well as the $\pm 3\sigma$ bounds. As expected, the EKF performs poorly in the second leg, where the mismatch between the true aircraft dynamics and the assumed EKF model is highest.

5,000 ft AGL, 2) a 57-km trajectory of a teardrop descent from 7,000 ft AGL down to touchdown at the runway, and 3) a 55-km trajectory of a holding pattern at about 15,000 ft AGL. Cellular SOPs produced remarkable navigation accuracy in all three flights, achieving a 3D position RMSE of 10.53 m, 4.96 m, and 15.44 m, respectively. These unprecedented results demonstrate the potential of cellular signals as a viable alternative to GNSS for high-altitude aircraft navigation. While the presented outcomes are encouraging, more accurate navigation results can be achieved by fusing cellular SOP observables with an INS.

> The EKF utilized a simple, yet effective continuous Wiener process acceleration model to describe the aircraft dynamics.

Acknowledgment

This work was supported in part by the Office of Naval Research under grant N00014-19-1-2511 and grant N00014-19-1-2613, in part by Sandia National Laboratories under award 1655264, in part by the National Science Foundation under grant 1929965, and in part by the U.S. Department of Transportation under grant 69A3552047138 for the Center for Automated Vehicles Research with Multimodal Assured Navigation University Transportation Center.

The authors would like to thank Edwards AFB and Holloman AFB for inviting the ASPIN Laboratory to conduct experiments on USAF aircraft in the "Signals of Opportunity for Navigation in Frequency-Forbidden Environments" flight campaign. The authors would like to thank Joshua Morales, Kimia Shamaei, Mahdi Maaref, Kyle Semelka, MyLinh Nguyen, and Trier Mortlock for their help in preparing for data collection. DISTRIBUTION STATEMENT A. Approved for public release; distribution is unlimited. 412TW-PA-20146.

About the Authors

Zaher (Zak) M. Kassas (zkassas@ieee.org) earned his B.E. degree in electrical engineering from the Lebanese American University, his M.S. degree in electrical and Computer Engineering from The Ohio State University, and his M.S.E. degree in aerospace engineering and Ph.D. degree in electrical and computer engineering from The University of Texas at Austin. He is a professor of Electrical and Computer Engineering at The Ohio State University, Columbus, OH 43210 USA, and director of the Autonomous Systems Perception, Intelligence, and Navigation Laboratory (ASPIN). He is also director of the U.S. Department of Transportation Center for Automated Vehicle Research with Multimodal Assured Navigation (CARMEN), focusing on navigation resiliency and security of highly automated transportation systems. His research interests include cyberphysical systems, estimation theory, navigation systems, autonomous vehicles, and intelligent transportation systems. He is a recipient of the 2018 National Science Foundation CAREER award, 2019 Office of Naval Research Young Investigator Program (YIP) award, 2022 Air Force Office of Scientific Research YIP award, 2018 IEEE Walter Fried Award, 2018 Institute of Navigation (ION) Samuel Burka Award, and 2019 ION Col. Thomas Thurlow Award. He is an associate editor of *IEEE Transactions on Aerospace and Electronic Systems* and *IEEE Transactions on Intelligent Transportation Systems*. He is a fellow of the ION and a Distinguished Lecturer of the IEEE Aerospace and Electronic Systems Society.

Joe Khalife (khalifej@uci.edu) earned his B.E. degree in electrical engineering and his M.S. degree in computer engineering from the Lebanese American University and his Ph.D. degree in electrical engineering and computer science from the University of California, Irvine. He was a postdoctoral fellow at the University of California, Irvine, and a member of the Autonomous Systems Perception, Intelligence, and Navigation (ASPIN) Laboratory, University of California, Irvine, CA 92697 USA. From 2012 to 2015, he was a research assistant at the Lebanese American University and has been a member of the ASPIN Laboratory since 2015. His research interests include opportunistic navigation, autonomous vehicles, and software-defined radio. He is a recipient of the 2016 IEEE/Institute of Navigation Position, Location, and Navigation Symposium Best Student Paper Award, 2018 IEEE Walter Fried Award, and 2021 IEEE AESS Robert T. Hill Best Dissertation Award. He is a Member of IEEE.

Ali A. Abdallah (abdalla2@uci.edu) earned his B.E. degree in electrical engineering from the Lebanese American University and M.S. degree in electrical engineering and computer science from the University of California, Irvine. He was a member of the Autonomous Systems Perception, Intelligence, and Navigation Laboratory, University of California, Irvine, CA 92697 USA. He is a recipient of the Best Student Paper Award at the 2020 IEEE/Institute of Navigation Position, Location, and Navigation Symposium. He is a Student Member of IEEE.

Chiawei Lee (chiawei.lee@us.af.mil) earned his B.S. degree in aerospace engineering from the University of California, Los Angeles, and his M.S. degree in aero/astro engineering from Stanford University. He is an assistant professor and instructor flight test engineer at the U.S. Air Force Test Pilot School, Edwards Air Force Base, Edwards, CA 93524 USA. He serves as the test management program director, overseeing about a dozen student and staff-led flight test projects each year. In addition, he is the chief test safety officer responsible for the safe execution of curriculum and flight test project safety packages.

Juan Jurado (jdjurado@icloud.com) earned his B.S. degree from Texas A&M University, his M.S. degree from the U.S. Air Force Test Pilot School, and M.S. and Ph.D. degrees from the Air Force Institute of Technology. He is a U.S. Air Force lieutenant colonel and the director of education at the U.S. Air Force Test Pilot School, Edwards Air Force Base, Edwards, CA 93524 USA. Previously, he served as director of engineering for the 413th Flight Test Squadron and oversaw various C-130, V-22, and H-1 flight test programs. His research interests include aircraft performance modeling, online sensor calibration, image processing, visual–inertial navigation, and statistical sensor management for multisensor navigation problems.

Steven Wachtel (steven.wachtel.1@us.af.mil) earned his B.S. degree in mechanical engineering from The Ohio State University, an M.S. degree in flight test engineering from the U.S. Air Force Test Pilot School, and an M.S. degree in systems engineering from the Air Force Institute of Technology. He is a U.S. Air Force captain and a flight test engineer assigned to the 780th Test Squadron at the U.S. Air Force Test Pilot School, Edwards Air Force Base, Edwards, CA 93524 USA.

Jacob Duede (jacob.duede@us.af.mil) earned his M.S. degree in engineering from the University of Arkansas and his M.S. degree in flight test engineering from Air University. He is a major in the U.S. Air Force and is with the U.S. Air Force Test Pilot School at Edwards Air Force Base, Edwards, CA 93524 USA. He was trained as a communication/navigation/mission systems apprentice on C-17 Globmaster II aircraft and stationed at McChord Air Force Base, WA. He graduated from the U.S. Air Force Academy as a commissioned officer with a B.S. in mechanical engineering. He attended the undergraduate pilot training at Columbus Air Force Base, MS. In 2020, he graduated from the U.S. Air Force Test Pilot School at Edwards Air Force Base. He is a senior pilot with more than 2,000 h.

Zachary Hoeffner (zachary.hoeffner.1@us.af.mil) earned his B.S degree in nuclear engineering from the U.S. Air Force Academy, his M.S. degree in flight test engineering from the U.S. Air Force Test Pilot School, his M.S. degree in engineering physics and applied physics from the Air Force Institute of Technology, and his M.S. degree in nuclear engineering from the Air Force Institute of Technology. He is a flight test engineer for the U.S. Air Force with the U.S. Air Force Test Pilot School at Edwards Air Force Base, Edwards, CA 93524 USA.

Thomas Hulsey (thomas.hulsey.2@us.af.mil) earned his B.S. degree in aerospace engineering from the Missouri University of Science and Technology, his M.S. degree in aeronautical engineering from the Air Force Institute of Technology, and his M.S. degree in experimental flight test engineering from the U.S. Air Force Test Pilot School. He is a U.S. Air Force Flight Commander of Operations Engineering with the U.S. Air Force Test Pilot School at Edwards Air Force Base, Edwards, CA 93524 USA.

Rachel Quirarte (rachel.quirarte@us.af.mil) earned her B.S. degree in aeronautical engineering from the U.S. Air Force Academy, her M.S. degree in flight test engineering from the U.S. Air Force Test Pilot School, and her M.S. degree in mechanical engineering from Rice University. She is a KC-46 and KC-135 programmatic flight commander and test pilot in the 418th Flight Test Squadron in the U.S. Air Force and is with the U.S. Air Force Test Pilot School at Edwards Air Force Base, Edwards, CA 93524 USA.

RunXuan Tay (rxtay@outlook.com) earned his B.S. degree in electrical engineering from the University of California, San Diego, and his M.S. degree in flight test engineering from the U.S. Air Force Test Pilot School. He is currently a test pilot at the Air Warfare Center, Republic of Singapore Air Force, Singapore, where he works on fixed-wing test programs.

References

[1] "ASRS database online," ASRS/NASA, Washington, DC, USA. [Online]. Available: https://asrs.arc.nasa.gov/search/database.html

[2] M. Harris, "FAA files reveal a surprising threat to airline safety," *IEEE Spectr.*, Jan. 2021. [Online]. Available: https://spectrum.ieee.org/faa-files-reveal-a-surprising-threat-to-airline-safety-the-us-militarys-gps-tests

[3] D. Miralles et al., "An assessment of GPS spoofing detection via radio power and signal quality monitoring for aviation safety operations," *IEEE Intell. Transp. Syst. Mag.*, vol. 12, no. 3, pp. 136–146, Jun. 2020, doi: 10.1109/MITS.2020.2994117.

[4] F. Dovis, L. Ruotsalainen, R. Toledo-Moreo, Z. Kassas, and V. Gikas, "Recent advancement on the use of global navigation satellite system-based positioning for intelligent transport systems," *IEEE Intell. Transp. Syst. Mag.*, vol. 12, no. 3, pp. 6–9, Jun. 2020, doi: 10.1109/MITS.2020.2994923.

[5] "An urgent need to address harmful interferences to GNSS," Int. Civil Aviation Org., Montreal, QC, Canada, Tech. Rep. A40-WP/188, May 2019. [Online]. Available: https://www.iata.org/contentassets/e45e5219cc8c4277a0e80562590793da/address-harmful-interferences-gnss.pdf

[6] A. Hansen et al., "Complementary PNT and GPS backup technologies demonstration report: Sections 1 through 10," John A. Volpe National Transportation Systems Center (US), U.S. Dept. Transp., Washington, DC, USA, no. DOT-VNTSC-20-07, Jan. 2021.

[7] M. Bartock et al., "Foundational PNT profile: Applying the cybersecurity framework for the responsible use of positioning, navigation, and timing (PNT) services," Nat. Inst. Standards Technol. (NIST), Gaithersburg, MD, USA, NISTIR 8323, Feb. 2021.

[8] Z. Kassas, "Position, navigation, and timing technologies in the 21st century," in *Navigation with Cellular Signals of Opportunity*, vol. 2, J. Morton, F. van Diggelen, J. Spilker Jr., and B. Parkinson, Eds. New York, NY, USA: Wiley, 2021, ch. 38, pp. 1171–1223.

[9] A. Abdallah, J. Khalife, and Z. Kassas, "Experimental characterization of received 5G signals carrier-to-noise ratio in indoor and urban environments," in *Proc. IEEE Veh. Technol. Conf.*, Apr. 2021, pp. 1–5, doi: 10.1109/VTC2021-Spring51267.2021.9448729.

[10] Z. Kassas, M. Maaref, J. Morales, J. Khalife, and K. Shamaei, "Robust vehicular localization and map matching in urban environments through IMU, GNSS, and cellular signals," *IEEE Intell. Transp. Syst. Mag.*, vol. 12, no. 3, pp. 36–52, Jun. 2020, doi: 10.1109/MITS.2020.2994110.

[11] M. Maaref and Z. Kassas, "Autonomous integrity monitoring for vehicular navigation with cellular signals of opportunity and an IMU," *IEEE Trans. Intell. Transp. Syst.*, vol. 23, no. 6, pp. 5586–5601, Jun. 2022, doi: 10.1109/TITS.2021.3055200.

[12] J. Khalife and Z. Kassas, "On the achievability of submeter-accurate UAV navigation with cellular signals exploiting loose network synchronization," *IEEE Trans. Aerosp. Electron. Syst.*, vol. 58, no. 5, pp. 4261–4278, Oct. 2022, doi: 10.1109/TAES.2022.3162770.

[13] J. Khalife and Z. Kassas, "Differential framework for submeter-accurate vehicular navigation with cellular signals," *IEEE Trans. Intell. Veh.*, early access, 2022, doi: 10.1109/TIV.2022.3187957.

[14] Z. Kassas, J. Khalife, A. Abdallah, and C. Lee, "I am not afraid of the GPS jammer: resilient navigation via signals of opportunity in GPS-denied environments," *IEEE Aerosp. Electron. Syst. Mag.*, vol. 37, no. 7, pp. 4–19, Jul. 2022, doi: 10.1109/MAES.2022.3154110.

[15] Y. Zeng, Q. Wu, and R. Zhang, "Accessing from the sky: A tutorial on UAV communications for 5G and beyond," *Proc. IEEE*, vol. 107, no. 12, pp. 2327–2375, Dec. 2019, doi: 10.1109/JPROC.2019.2952892.

[16] X. Cai et al., "An empirical air-to-ground channel model based on passive measurements in LTE," *IEEE Trans. Veh. Technol.*, vol. 68, no. 2, pp. 1140–1154, Feb. 2019, doi: 10.1109/TVT.2018.2886961.

[17] W. Khawaja, I. Guvenc, D. Matolak, U. Fiebig, and N. Schneckenburger, "A survey of air-to-ground propagation channel modeling for unmanned aerial vehicles," *IEEE Commun. Surveys Tuts.*, vol. 21, no. 3, pp. 2361–2391, Thirdquarter 2019, doi: 10.1109/COMST.2019.2915069.

[18] K. Matheou et al., "Analysis of at-altitude LTE power spectra for small unmanned aircraft system C2 communications," in *Proc. Integr. Commun., Navig. Surveillance Conf.*, Apr. 2019, pp. 1–12, doi: 10.1109/ICNSURV.2019.8735287.

[19] X. Cai et al., "Low altitude air-to-ground channel characterization in LTE network," in *Proc. Eur. Conf. Antennas Propag.*, Apr. 2019, pp. 1–5.

[20] B. Van Der Bergh, A. Chiumento, and S. Pollin, "LTE in the sky: trading off propagation benefits with interference costs for aerial nodes," *IEEE Commun. Mag.*, vol. 54, no. 5, pp. 44–50, May 2016, doi: 10.1109/MCOM.2016.7470934.

[21] I. Kovacs, R. Amorim, H. Nguyen, J. Wigard, and P. Mogensen, "Interference analysis for UAV connectivity over LTE using aerial radio measurements," in *Proc. IEEE Veh. Technol. Conf.*, Sep. 2017, pp. 1–6.

[22] R. Amorim, J. Wigard, I. Kovacs, and T. Sorensen, "UAV communications for 5G and beyond," in *Performance Enhancements for LTE-Connected UAVs: Experiments and Simulations*, Y. Zeng, I. Guvenc, R. Zhang, G. Geraci, and D. Matolak, Eds. New York, NY, USA: Wiley, 2021, ch. 5, pp. 139–161.

[23] E. Teng, J. Diogo Falcao, and B. Iannucci, "Holes-in-the-sky: A field study on cellular-connected UAS," in *Proc. Int. Conf. Unmanned Aircraft Syst.*, Jun. 2017, pp. 1165–1174, doi: 10.1109/ICUAS.2017.7991402.

[24] X. Lin et al., "The sky is not the limit: LTE for unmanned aerial vehicles," *IEEE Commun. Mag.*, vol. 56, no. 4, pp. 204–210, Apr. 2018, doi: 10.1109/MCOM.2018.1700643.

[25] G. Athanasiadou, M. Batistatos, D. Zarbouti, and G. Tsoulos, "LTE ground-to-air field measurements in the context of flying relays," *IEEE Wireless Commun.*, vol. 26, no. 1, pp. 12–17, Feb. 2019, doi: 10.1109/MWC.2018.1800225.

[26] A. Abdalla and V. Marojevic, "Communications standards for unmanned aircraft systems: The 3GPP perspective and research drivers," *IEEE Commun. Standards Mag.*, vol. 5, no. 1, pp. 70–77, Mar. 2021, doi: 10.1109/MCOMSTD.001.2000032.

[27] H. Maattanen, "3GPP standardization for cellular-supported UAVs," in *UAV Communications for 5G and Beyond*, Y. Zeng, I. Guvenc, R. Zhang, G. Geraci, and D. Matolak, Eds. New York, NY, USA: Wiley, 2021, ch. 6, pp. 163–180.

[28] E. Kim and Y. Shin, "Feasibility analysis of LTE-based UAS navigation in deep urban areas and DSRC augmentation," *Sensors*, vol. 19, no. 19, pp. 4192–4207, Apr. 2019, doi: 10.3390/s19194192.

[29] Z. Kassas et al., "Assessment of cellular signals of opportunity for high altitude aircraft navigation," *IEEE Aerosp. Electron. Syst. Mag.*, vol. 37, no. 10, pp. 4–19, Oct. 2022, doi: 10.1109/MAES.2022.3187142.

[30] X. Li and V. Jilkov, "Survey of maneuvering target tracking. Part I: Dynamic models," *IEEE Trans. Aerosp. Electron. Syst.*, vol. 39, no. 4, pp. 1333–1364, Oct. 2003, doi: 10.1109/TAES.2003.1261132.

[31] J. Morales and Z. Kassas, "Tightly-coupled inertial navigation system with signals of opportunity aiding," *IEEE Trans. Aerosp. Electron. Syst.*, vol. 57, no. 3, pp. 1930–1948, Jun. 2021, doi: 10.1109/TAES.2021.3054067.

[32] J. Barnes et al., "Characterization of frequency stability," *IEEE Trans. Instrum. Meas.*, vol. IM-20, no. 2, pp. 105–120, May 1971, doi: 10.1109/TIM.1971.5570702.

[33] J. Khalife, K. Shamaei, and Z. Kassas, "Navigation with cellular CDMA signals – Part I: Signal modeling and software-defined receiver design," *IEEE Trans. Signal Process.*, vol. 66, no. 8, pp. 2191–2203, Apr. 2018, doi: 10.1109/TSP.2018.2799167.

[34] K. Shamaei and Z. Kassas, "LTE receiver design and multipath analysis for navigation in urban environments," *Navig., J. Inst. Navig.*, vol. 65, no. 4, pp. 655–675, Dec. 2018, doi: 10.1002/navi.272.

[35] J. Khalife and Z. Kassas, "Opportunistic UAV navigation with carrier phase measurements from asynchronous cellular signals," *IEEE Trans. Aerosp. Electron. Syst.*, vol. 56, no. 4, pp. 3285–3301, Aug. 2020, doi: 10.1109/TAES.2019.2948452.

[36] J. Morales and Z. Kassas, "Optimal collaborative mapping of terrestrial transmitters: Receiver placement and performance characterization," *IEEE Trans. Aerosp. Electron. Syst.*, vol. 54, no. 2, pp. 992–1007, Apr. 2018, doi: 10.1109/TAES.2017.2773238.

[37] M. Yeddanapudi, Y. Bar-Shalom, and K. Pattipati, "IMM estimation for multitarget-multisensor air traffic surveillance," *Proc. IEEE*, vol. 85, no. 1, pp. 80–96, Jan. 1997, doi: 10.1109/5.554210.

[38] A. Mohamed and K. Schwarz, "Adaptive Kalman filtering for INS/GPS," *J. Geodesy*, vol. 73, no. 4, pp. 193–203, May 1999, doi: 10.1007/s001900050236.

[39] P. Hanlon and P. Maybeck, "Multiple-model adaptive estimation using a residual correlation Kalman filter bank," *IEEE Trans. Aerosp. Electron. Syst.*, vol. 36, no. 2, pp. 393–406, Apr. 2000, doi: 10.1109/7.845216.

[40] C. Hide, T. Moore, and M. Smith, "Adaptive Kalman filtering for low-cost INS/GPS," *J. Navig.*, vol. 56, no. 1, pp. 143–152, Jan. 2003, doi: 10.1017/S0373463302002151.

[41] W. Ding, J. Wang, C. Rizos, and D. Kinlyside, "Improving adaptive Kalman estimation in GPS/INS integration," *J. Navig.*, vol. 60, no. 3, pp. 517–529, Sep. 2007, doi: 10.1017/S0373463307004316.

[42] M. Yu, "INS/GPS integration system using adaptive filter for estimating measurement noise variance," *IEEE Trans. Aerosp. Electron. Syst.*, vol. 48, no. 2, pp. 1786–1792, Apr. 2012, doi: 10.1109/TAES.2012.6178100.

[43] Z. Kassas, V. Ghadiok, and T. Humphreys, "Adaptive estimation of signals of opportunity," in *Proc. ION GNSS Conf.*, Sep. 2014, pp. 1679–1689.

[44] J. Dunik, O. Straka, O. Kost, and J. Havlik, "Noise covariance matrices in state-space models: A survey and comparison of estimation methods—Part I," *Int. J. Adaptive Control Signal Process.*, vol. 31, no. 11, pp. 1505–1543, May 2017, doi: 10.1002/acs.2783.

[45] J. Dunik, O. Kost, O. Straka, and E. Blasch, "Navigation and estimation improvement by environmental-driven noise mode detection," in *Proc. IEEE/ION Position, Location, Navig. Symp.*, 2020, pp. 925–932.

ITS